Aeolian Saltation and Small-Scale Bedform Dynamics in a Large Eddy Simulation Domain

FPA Liqui Lung[a,*], S de Vries[a] and HJJ Jonker[b,a]

[a]*Delft University of Technology, Dept of Geoscience & Remote Sensing, Stevinweg 1, 2628 CN Delft, The Netherlands*
[b]*Whiffle Weather Finecasting, Molengraaffsingel 12-14, 2629 JD Delft, The Netherlands*

ARTICLE INFO

Keywords:
Aeolian saltation
Turbulence
Ripple formation

ABSTRACT

In this paper we introduce a setup to investigate aeolian saltation and surface dynamics on a centimetre spatial resolution and a sub second temporal resolution. We develop a Lagrangian saltation model and a high-resolution surface model, which we couple to each other and to a turbulence resolving large eddy simulation model. The simulated transport takes place primarily in the form of aeolian streamers, bursts of elongated transport structures parallel to the wind field, which result in a mass flux signal that is highly heterogeneous both in space and time. The temporal frequency responses up to 1 Hz of the mass flux and wind field share the same characteristics, which indicates a coupling between the two. The system can be in equilibrium, during which the stress profiles induced by the particles, the turbulent fluxes and the imposed large scale pressure gradient balance each other. A bimodal shape is found in the mass flux profile, in which we can distinguish an upper and lower saltation layer. The upper layer is associated with a transitional phase between transport by saltation and suspension that exists in the aeolian streamers. Furthermore, The setup is able to simulate ripples, although future research is needed to investigate the mechanisms that influence the final shape of the ripples.

1. Introduction

Aeolian (wind driven) sediment transport takes place on a wide range of temporal and spatial scales. On these scales the transport mode, wind characteristics and the interactions with the environment differ. On a synoptic scale, storms can transport vast amounts of dust which can influence the radiation budget (Miller et al., 2004), redistribute nutrients (Jickells et al., 2005) and pose human health risks (Goudie, 2020). On a more regional scale, sediment transport threatens large areas with desertification (Shao, 2008) while dune dynamics can be important for coastal defence measures (Vries et al., 2012). There are three main transport modes (Bagnold, 1941). Dust particles can be sufficiently small to be kept in suspension by turbulent eddies, which allows for long distance transport. Sand is too heavy to stay suspended and is mostly transported in a hopping motion over the surface which is known as saltation. On impact, saltating particles have the ability to set heavier particles in a sliding and rolling motion over the surface. This is known as creep. The impact of saltating particles is also an important factor for the initialisation of dust into the wind field, as the strong interparticle forces of dust often prevent direct initialisation by the wind field (Gillette, 1974; Shao et al., 1993).

A precise understanding of the saltation mechanisms will benefit the knowledge of aeolian processes in general and could help with addressing the problems described above. Therefore, extensive research has been conducted in the field of aeolian saltation. Bagnold (1941) gives the first full description of saltation and derives an analytical parametrisation that links the surface shear velocity to the total mass flux. Many improvements have been made ever since (Sherman and Li, 2012). These parametrisations have the ability to produce fast results that agree well to wind tunnel experiments conducted by e.g. Iversen and Rasmussen (1999); Creyssels et al. (2009); Li et al. (2010); Ho et al. (2011). They however, give no information on the retardation of the wind field or the interactions with the surface. To this end, more advanced numerical models have been developed using a continuum description, which are able to accurately simulate dune dynamics over long time scales (Sauermann et al., 2001; Kroy et al., 2002). The mass flux in these models is often in equilibrium with the local wind field, or forced towards an equilibrium with a set adaptation scale in time and/or space (Sauermann et al., 2001; de Vries et al., 2014). To investigate the transitional phase towards a possible equilibrium, the role of turbulence and the momentum exchange between the particles and the wind field, a different approach is required. For this reason recent studies have coupled a Lagrangian particle description to a turbulence resolving wind model (Tong and Huang, 2012; Huang et al., 2020). The setup is able to resolve the transitional phases and the influence of turbulence on saltation. The individual particle description does come with computational costs, that put a restraint on the domain size and simulation time, which makes the implementation of an active surface scheme for ripple formation not feasible yet.

For this research a model is developed with the aim to resolve the effects of turbulence on the particle trajectories while still allowing simulation times sufficient for small-scale surface structures to develop and grow. To achieve this goal we develop a scaled Lagrangian particle (SLP) model and a high-resolution surface (HRS) model, which we embed in a turbulence resolving large eddy simulation (LES) model. This will help to close the gap between the available continuum and Lagrangian models. We will give an extensive description of the model together with the results it produces.

f.p.a.liquilung-1@tudelft.nl (F. Liqui Lung)

2. Model description

To be able to simulate aeolian saltation and small-scale surface dynamics, this research introduces a model that consists of three sub-models; a large eddy simulation model (LES), a scaled Lagrangian particle (SLP) model and a high-resolution surface (HRS) model. All three sub-models are two way coupled to each other with feedback mechanisms visualised in fig. 1. The LES model is used to resolve the

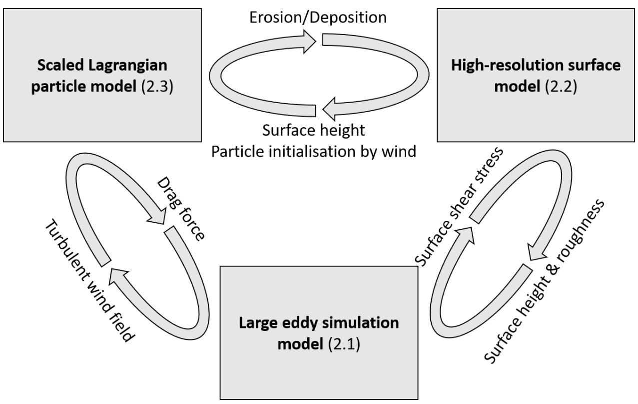

Figure 1: Schematic visualisation of the model constituents and feedback mechanisms.

large scale structures of the turbulent wind field and will be discussed in sec. 2.1. The LES allows for the simulation of streaky structures (Wyngaard, 2011), while still being able to simulate a domain with an extent of $L_x \times L_y \times L_z = 8\times4\times4$ m and a resolution of $\Delta x \times \Delta y \times \Delta z = 5 \times 5 \times 2$ cm for a time period of 20 minutes.

The LES resolution is sufficient to resolve the energy-containing turbulent wind structures, but is too course to capture small-scale surface features. For this reason the HRS model is developed, which will be discussed in sec. 2.2. The HRS model has the same spatial extent as the LES, but with a resolution of $\Delta x^s \times \Delta y^s = 1 \times 1$ cm. The HRS model resolves the surface topography by enforcing conservation of mass using a local sediment budget and is able to initialise particles into saltation when there is sufficient wind induced surface shear stress.

To simulate saltation the SLP model is developed, which will be discussed in sec. 2.3. The SLP description resolves particle trajectories, for which it uses the turbulent wind field from the LES model for the drag force and the surface topography from the HRS model for the impact locations. However, for the given domain size and simulation time it would not be feasible to simulate each individual particle. Instead, a similar approach to the super-droplet method is used, which was introduced by Shima et al. (2009) for the simulation of cloud microphysics. In the SLP description each simulated particle represents multiple, ψ, physical particles. All forces acting on the simulated particle are calculated as if it was a single physical particle and all feedback forces on the wind field and surface are obtained using the scaling factor ψ.

2.1. Large eddy simulation model

A large eddy simulation (LES) model is used to simulate the wind field. LES models are well established in the field of atmospheric science and are often used to simulate the planetary boundary layer (Wyngaard, 2011), in which the effects of turbulent eddies are dominant. They rely on the assumption that most turbulent kinetic energy is contained in the large eddies, motivating a description that resolves the large eddies and parametrises the eddies that are subgrid, smaller than the LES gridsize. LES can therefore be placed between direct numerical simulations, which try to resolve all turbulent scales down to the viscous scale, and mesoscale simulations that need to parametrise all turbulent effects. In this research we use the LES model GRASP, which is a GPU based LES model (Schalkwijk et al., 2015) that originates from the Dutch Atmospheric Large Eddy Simulation (DALES) model (Heus et al., 2010).

The simulations take place in a neutral dry boundary layer, which means that there are no temperature and humidity effects. The LES model solves the filtered incompressible Navier Stokes equations.

$$\frac{\partial u_\alpha}{\partial x_\alpha} = 0 \tag{1}$$

$$\rho \frac{\partial u_i}{\partial t} = -\rho \frac{\partial u_i u_\alpha}{\partial x_\alpha} - \frac{\partial \pi}{\partial x_i} - \frac{\partial \tau_{i\alpha}}{\partial x_\alpha} + F_i \tag{2}$$

Equations (1) & (2) represent respectively the conservation of mass and momentum. Greek subscript indices indicate that the Einstein summation convention is used. The wind velocity vector $\mathbf{u}$ is the filtered mean wind velocity. The influence of subgrid velocity variations, $\mathbf{u}'$, are captured in a stress tensor, τ. The hydrostatic part of the stress tensor forms together with the filtered mean pressure, p, the modified pressure π.

$$\pi = p + \frac{\rho}{3}\left\langle \left(u'_\alpha\right)^2 \right\rangle \tag{3}$$

In (3) $\langle\ \rangle$ denotes an LES gridcell average and ρ is the density of air. The deviatoric part of the stress tensor is represented in τ_{ij}.

$$\tau_{ij} = \rho \left\langle u'_i u'_j \right\rangle - \frac{\rho}{3}\left\langle \left(u'_\alpha\right)^2 \right\rangle \tag{4}$$

We use the subgrid scheme of Sullivan et al. (1994) to obtain $\left\langle u'_i u'_j \right\rangle$ and we ignore the effects of viscous stresses as they are negligible compared to the subgrid turbulent stresses. The surface shear stress is often expressed in terms of a friction velocity.

$$\tau_0 = \sqrt{\tau_{13}^2 + \tau_{23}^2} = \rho u_*^2 \tag{5}$$

The friction velocity is obtained with the Monin-Obukhov (MO) surface routine for a neutral boundary (Obukhov, 1971).

$$u_* = \frac{\kappa \left|\mathbf{u}^{\mathrm{h}}\left(\Delta z/2\right)\right|}{\log\left(\frac{\Delta z/2}{z_{0m}}\right)} \tag{6}$$

In (6) κ is the Von Kármán constant and is taken as $\kappa = 0.41$, $|\mathbf{u}^{\mathrm{h}}| = \sqrt{u_1^2 + u_2^2}$ the magnitude of the horizontal wind velocity which is taken at the lowest gridcell centre above the bottom of the domain ($\Delta z/2$) and z_{0m} the surface roughness for momentum. F_i contains all body forces.

$$F_i = -\frac{\partial P}{\partial x_i} + F_i^{\mathrm{p}} \tag{7}$$

In (7) $\frac{\partial P}{\partial x_i}$ is an imposed large scale pressure gradient and F_i^{p} the particle induced force. The large scale pressure gradient, $\frac{\partial P}{\partial x_i}$, is constant in space and time and is responsible for driving the main flow. The modified pressure, π, which contains the local pressure p, is responsible for enforcing continuity (1). For this research the Coriolis force is not taken into account. When there are no particle forces present, the simulation setup is equivalent to a channel flow. For channel flows the friction velocity can be linked to the large scale pressure gradient (Westerweel et al., 2016).

$$u_* = \sqrt{\frac{L_z}{\rho}\left|\frac{\partial P}{\partial x}\right|} \tag{8}$$

In (8) L_z represents the domain height. The derivation is for a stationary and horizontally homogeneous turbulent flow. For these assumptions to hold, the LES needs sufficient spinup time.

2.2. High-resolution surface model

To be able to simulate surface dynamics on a higher resolution than the LES gridsize, we develop a high-resolution surface (HRS) model. The HRS grid is aligned with the LES grid and is used to couple the local surface topography to the LES model. The topography is obtained by enforcing mass conservation using a local sediment budget. The HRS model is also responsible for particle initialisation by wind, for which it uses the wind induced surface shear stress. Initialisation by splashing is implemented in the SLP model, sec. 2.3.5.

2.2.1. Surface grid

The HRS grid spans the same surface area as the LES grid, but with a resolution that is an integer factor, λ, higher than the resolution of the LES grid. Figure 2 shows how the HRS grid (dashed black lines) aligns with the LES grid (black lines) for $\lambda = 3$ in a single LES grid cell. Each HRS gridcell has a centre height, h. A zeroth order continuous surface is obtained using a triangular interpolation method, which is shown by the grey shading in fig. 2. The obtained triangle faces are used to find the impact locations of the particles with the local surface, such that the particles directly feel the local surface structures. This allows for impact shadow zones, which are crucial for the formation and growth of ripples, Bagnold (1941). Subgrid variations to the HRS grid are captured in a homogeneous surface roughness, z_{0m}^{s}.

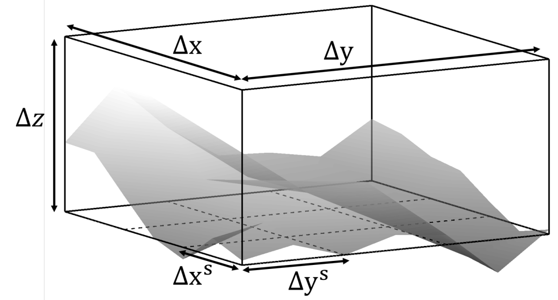

Figure 2: Visualisation of the HRS and LES grid alignment in a single LES gridcell for a refinement factor of $\lambda = 3$. The solid black lines show a LES gridcell, the dashed lines show the HRS grid and the shading shows the surface topography, h.

2.2.2. Large eddy simulation surface coupling

The local surface topography is coupled to the LES model via a subgrid implementation and immersed boundary conditions (Tomas et al., 2015). We start by defining the LES surface roughness in terms of the HRS topography.

$$z_{0m} = \max\left(\sqrt{\left\langle\left[h - \langle h\rangle\right]^2\right\rangle},\ z_{0m}^{\mathrm{s}}\right) \tag{9}$$

In (9) $\langle\ \ \rangle$ denotes the average over an LES gridcell. Subsequently, we define the zero wind speed level.

$$h_0 = \langle h\rangle + z_{0m} \tag{10}$$

Whenever h_0 exceeds an LES gridcell centre, an immersed boundary is created in the gridcell. The immersed boundary moves the bottom boundary height, h_{b}, to the top of the LES gridcell. The discrete nature of immersed boundary conditions creates a discrepancy between the zero wind level height and the bottom boundary height. To allow for a continuous variation, a displacement height is defined.

$$h_{\mathrm{d}} = \langle h\rangle - h_{\mathrm{b}} \tag{11}$$

The displacement height is used to adjust the MO surface routine (6).

$$u_* = \frac{k\left|\mathbf{u}^{\mathrm{h}}\left(\Delta z/2 + h_b\right)\right|}{\log\left(\frac{\Delta z/2 - h_{\mathrm{d}}}{z_{0m}}\right)} \tag{12}$$

The adjustments corrects for the discrepancy between the zero wind level height and the bottom boundary height in the surface shear stress calculation. To allow for "negative" immersed boundary conditions the surface is lifted by an offset Δz_0. Figure 3 summarizes the implementation of the subgrid topography into the LES for $\lambda = 3$ in a schematic 2D visualisation.

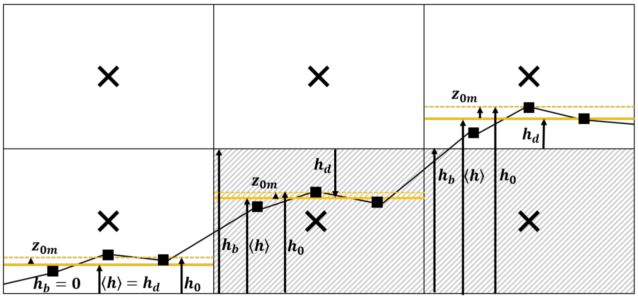

Figure 3: 2D schematic visualisation of the subgrid topography implementation into the LES for $\lambda = 3$. The crosses represent the LES grid centres and the surrounding box the grid edges. The gray colored cells represent the immersed boundary conditions. The solid squares are the HRS heights, h. The yellow dashed line shows the zero velocity height, h_0, given by the sum of the mean LES gridcell surface height, $\langle h \rangle$ (yellow line), and the LES roughness height, z_{0m}. The displacement height, h_d, is given by the difference between the mean height and the bottom boundary height, h_b.

2.2.3. Surface sediment budget

When particles are initialised into saltation, either by the local wind field or by splashing, mass is removed from the surface. Similarly mass is added to the surface, when particles are removed from saltation and deposited on the surface. A deficit in erosion and deposition will result in a local surface height change.

$$\Delta h = \frac{\psi_\alpha^{\mathrm{d}} m_\alpha^{\mathrm{d}} - \psi_\alpha^{\mathrm{e}} m_\alpha^{\mathrm{e}}}{(1-\phi)\rho^{\mathrm{p}} \Delta x^{\mathrm{s}} \Delta y^{\mathrm{s}}} \tag{13}$$

In (13) m_α and ψ_α are the mass and scaling factor of simulation particle α and ϕ is the surface porosity, which describes the void/volume ratio of the surface. The superscript d and e denote respectively deposited or initialised particles. The Greek subscripts indicate that the Einstein summation convention is used.

2.2.4. Particle initialisation by wind

Particles can be initialised into saltation by the local wind field. The rate of initialisation is based on a local momentum balance. A fraction, χ, of the momentum loss by the wind field at the surface as a result of the surface shear stress is used to accelerate particles to their initial velocity. We define a friction velocity at the HRS scale.

$$u_*^{\mathrm{s}} = \frac{\kappa \left| \mathbf{u}^{\mathrm{h}} \left(\Delta z_{\mathrm{ref}} + h \right) \right|}{\log \left(\frac{\Delta z_{\mathrm{ref}}}{z_{0m}} \right)} \tag{14}$$

The surface shear stress on the HRS grid is defined similar to the surface shear stress on the LES grid, (12). The only difference is that a wind velocity at a fixed height distance, Δz_{ref}, from the HRS height, h, is used.

The wind field is only able to initialise particles if the friction velocity is larger than a threshold value, u_*^T, for which the relation of Shao and Lu (2000) is used.

$$u_*^T = C^T \sqrt{\frac{\rho^{\mathrm{p}} - \rho}{\rho} d g + \frac{\gamma^T}{d \rho}} \tag{15}$$

In (15) C^T is a scaling constant and γ^T is a constant force that accounts for interparticle interactions. We can now define the wind initialisation rate.

$$n = \frac{\chi \Delta x^{\mathrm{s}} \Delta y^{\mathrm{s}} \rho \left(u_*^{\mathrm{s}} \right)^2}{m u_3^t} H \left(u_*^{\mathrm{s}} - u_*^T \right) \tag{16}$$

In (16) H is the Heaviside step function that takes the threshold friction velocity into account. An initialisation velocity is required, for which we choose the terminal velocity, u_*^{t}, as recent studies showed that the initial velocity is independent on the friction velocity (Kok et al., 2012). The terminal velocity is the steady state velocity of the particles for which the drag force and gravitational force cancel each other and will be derived in sec. 2.3.2. The initialisation rate, n, is integrated over time till the total number of initialised particles is equal or larger than a set minimum scale factor, ψ_{min}. When this limit is reached a simulated particle is initialised, with an scale parameter, ψ, equal to the current number of integrated physical particles. After the particle is initialised the integration starts over again. Note that n is the initialisation rate by the local wind field only. Particles are also initialised by splashing, which is implemented in the SLP model, sec. 2.3.5.

2.3. Scaled Lagrangian particle model

A scaled Lagrangian particle (SLP) model is developed to solve the trajectories of the saltating particles. The wind field from the LES model is used to obtain a force balance for the particles. The resulting equations of motions are integrated to determine the particle trajectories, which are subject to boundary conditions imposed on the surface and sides of the domain. Upon impact, particles can be removed from the SLP model and deposited on the surface and new particles can be initialised by splashing. The acceleration of the saltating particles results in a particle induced force in the LES momentum balance (2). To reduce the computational costs each simulated particle represents multiple, ψ, physical particles. The forces acting on the simulated particle are calculated for a single physical particle, which results in realistic particle trajectories. When effects such as erosion, deposition or drag on the wind field are communicated to the LES and HRS models, the scaling factor is used to obtain the effect of ψ physical particles.

2.3.1. Particle force balance

The particle's trajectory is determined by the aerodynamic drag force and the gravitational force. The drag force is obtained using the wind vector in the particle's reference frame and the drag equation.

$$F_i^{\mathrm{D}} = \frac{1}{8} C^{\mathrm{D}} \rho d^2 \left| u_i - u_i^{\mathrm{p}} \right| \left(u_i - u_i^{\mathrm{p}} \right) \tag{17}$$

In (17) $\mathbf{u}^{\mathrm{p}}$ is the particle velocity, d the particle diameter, $\mathbf{u}$ the filtered wind velocity interpolated from the LES grid to the particle's location. C^{D} is the drag coefficient for which the empirical relation of Goossens (2019) is used.

$$C^{\mathrm{D}} = \frac{24}{Re} + 0.44 \tag{18}$$

The drag coefficient depends on the particle Reynolds number (e.g. Bagnold, 1941).

$$Re = \frac{\rho d \left|\mathbf{u} - \mathbf{u}^{\mathrm{p}}\right|}{\mu} \tag{19}$$

In (19) μ is the viscosity of air. The above description neglects the influence of subgrid velocity variations since $\mathbf{u}$ is the filtered LES wind velocity. However, Richter et al. (2019) argued that the interaction between subgrid turbulence and heavy particles can be neglected. Interparticle forces, such as collisions and electrostatic forces, lift forces and Magnus effects are also not taken into account, because it can be argued that these play a secondary role compared to the aerodynamic drag force and the gravitational force (e.g. Kok et al., 2012).

2.3.2. Particle path integration

Using (17) for the aerodynamic drag force, we define the equations of motion for a simulated particle.

$$\frac{du_i^p}{dt} = a_i^{\mathrm{p}} = \frac{F_i^{\mathrm{D}}}{m} - g\delta_{i3} \tag{20}$$

In (20) $\mathbf{a}^{\mathrm{p}}$ is the particle acceleration and δ_{ij} the delta dirac function. The equations of motion are integrated using a forward Euler integration scheme, which is applied for each third order Runga-Kutta time stage as implemented by the LES model. The time step is determined by the stability criteria present in the LES model and is in the order of 1 ms. The equations of motion can also be used to define the terminal velocity of the particles, which is used as the initialisation velocity for particles initialised by the wind field (16).

$$u_3^{\mathrm{t}} \Leftarrow \frac{\partial u_3^{\mathrm{p}}}{\partial t} = \frac{F_3^D}{m} - g = 0 \tag{21}$$

Using (17) together with the parametrisation of C^D (18), the terminal velocity, u_3^{t}, can be obtained from (21).

2.3.3. Boundary conditions

Similar to the LES model, periodic boundary conditions are imposed at the lateral boundaries of the domain. At the top of the domain no conditions need to be specified, as the particles only live in the lower sections of the domain. At the surface a set of conditions is imposed that, upon impact, alter the velocity vector of the incoming particle. Whenever an impact is within the particle's integrated path, the time step is split into two:

1. The particle's trajectory is integrated till the impact location, where the boundary conditions are applied.
2. The particle's trajectory is integrated for the remaining time step.

This process is repeated till the particle's local time equals the LES time. A particle can therefore have multiple impacts in a single LES time stage. At the surface a momentum balance is set, in which the incoming particle loses a fixed fraction of its momentum to the surface, ζ^{s}, and a fixed fraction to another particle, ζ^{p}, which can subsequently be initialised into saltation. The remaining momentum is distributed over the velocity components of the particle. A fixed angle, α, sets the angle between the horizontal and the velocity vector after impact. The angle between the positive x direction and the velocity vector, β, is held the same as before the impact, fig. 4. Using α and β we define a scaling vector $\mathbf{c}$.

$$\mathbf{c} = \begin{bmatrix}\cos(\alpha)\cos(\beta) & \cos(\alpha)\sin(\beta) & \sin(\alpha)\end{bmatrix} \tag{22}$$

The scaling vector $\mathbf{c}$ is used to define the velocity vector after impact.

$$u_i^{\mathrm{r}} = c_i \left|\mathbf{u}^{\mathrm{i}}\right| (1 - \zeta^s - \zeta^p) \tag{23}$$

In (23) $\mathbf{u}^{\mathrm{i}}$ is the velocity of the incoming particle and $\mathbf{u}^{\mathrm{r}}$ the velocity of that particle after the surface reflection.

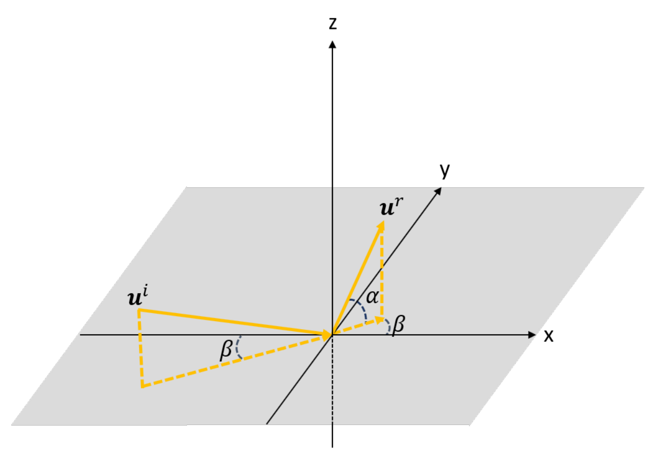

Figure 4: Visualisation of the velocity vectors before, $\mathbf{u}^{\mathrm{i}}$, and after impact, $\mathbf{u}^{\mathrm{r}}$.

2.3.4. Deposition

A particle is removed from the SLP model and deposited on the surface if its vertical velocity component after impact is smaller than a threshold velocity, $u_3^{\mathrm{r}} < u_3^T$. The threshold velocity is defined by an energy balance, such that the corresponding kinetic energy equals the potential energy over a set height difference. The height difference is defined as the maximum of the HRS grid roughness and the difference between the zero wind level height and the local surface height.

$$\Delta h_{\min} = \max\left[z_{0m}^{\mathrm{surf}},\ h_0 - h\right] \tag{24}$$

The height difference can be interpreted as the minimum vertical distance the particle needs to travel to be able to obtain momentum from the wind field. Using the minimum height difference the threshold velocity is defined.

$$u_3^{\mathrm{T}} = \sqrt{2g\Delta h_{\mathrm{min}}} \tag{25}$$

2.3.5. Particle initialisation by splashing

The momentum transferred to a new particle can initialise the particle if it corresponds to an initial vertical velocity greater than the threshold velocity defined in (25). The splashed particle is initialised in the same direction as the reflected particle, but with a velocity that corresponds with the obtained momentum.

$$u_i^{\mathrm{s}} = c_i \frac{m^{\mathrm{i}} \left|\mathbf{u}^{\mathrm{i}}\right| \zeta^{\mathrm{p}}}{m^{\mathrm{s}}} \tag{26}$$

In (26) $\mathbf{u}^{\mathrm{s}}$ and m^{s} are the velocity and mass of the splashed particle and $\mathbf{u}^{\mathrm{i}}$ and m^{i} the velocity and mass of the incoming particle. $\mathbf{c}$ is given by (22). The scaling parameter of the initialised particle, ψ, is the same as the scaling parameter of incoming particle. This approach is a simplified version of more advanced splash functions (e.g Kok and Rennó, 2009) in the limit where the ratio splashed to incoming particles is equal to one.

2.3.6. Particle induced force

Conservation of momentum requires that a simulated particle exerts a force on the wind field, $\mathbf{F}^{\mathrm{p}}$ (7), that is opposite in direction to the aerodynamic drag force, $\mathbf{F}^{D}$ (17), and scaled in magnitude by the scaling factor, ψ.

$$F_i^{\mathrm{p}} = -\frac{\psi F_i^D}{\Delta x \Delta y \Delta z} \tag{27}$$

In (27) Δx, Δy and Δz are the LES grid spacing in the x, y and z direction respectively. The momentum loss of the wind field due to the particle influence is spread equally over the LES gridcell occupied by the particle.

3. Simulation settings

3.1. Large eddy simulation settings

We simulate five channel flows in a $L_x \times L_y \times L_z = 8 \times 4 \times 4\ m$ domain for $t^{\mathrm{sim}} = 20$ minutes with different constant large scale pressure gradients, $\frac{\partial P}{\partial x}$. The large scale pressure gradients correspond via (8) to friction velocities of $u_* = 0.3, 0.4, 0.5, 0.6, 0.7\ m/s$. The initial average LES roughness for the simulations are respectively $z_{0m}^{\mathrm{spin}} = 0.75, 1, 1.25, 2, 2.5\ mm$. The roughness is implemented by applying a random normally distributed surface perturbation with a standard deviation equal to the roughness. Each simulation has a spinup simulation of $t^{\mathrm{spin}} = 5$ minutes before the saltation simulation starts. The LES settings are summarised in tab. 1.

3.2. Saltation settings

The settings used for the saltation simulation are summarised in tab. 2. The particle diameter is set to $d = 0.25\ mm$, which is often used as a reference diameter for sand (e.g. Bagnold, 1941). The density is set equal to the density of quartz $\rho^p = 2650\ kg/m^3$ (e.g. Bagnold, 1941). The terminal velocity for these particles is around $u_3^{\mathrm{t}} = 0.96\ m/s$. For the momentum balance at the surface fractions are used based on previous research summarised by Kok et al. (2012). A surface loss factor of, $\zeta^{\mathrm{s}} = 0.3$, and a transfer factor of $\zeta^{\mathrm{p}} = 0.15$, are used. A particle retains thus 55% of its momentum after impact. The saltation angle with respect to the horizontal is set to $\alpha = 45$ degrees, which is in the range of angles described by Kok et al. (2012). A surface porosity of $\phi = 0.4$ is chosen, which is a good representation of desert sand (e.g. Kolbuszewski et al., 1950). The momentum fraction used to activate particles into saltation is set to $\xi = 0.05$. The parameters for the initialisation friction velocity threshold, are set to the values given by Kok and Rennó (2006), $C^T = 0.111$ and $\gamma^T = 2.9 \cdot 10^{-4}\ N/m$. The subgrid surface roughness is set to $z_{0m}^{\mathrm{s}} = 0.01\ mm$, which is about 1/30 of the particle diameter, a commonly used roughness scale (e.g. Kok et al., 2012). The minimum scale factor is chosen such that the maximum amount of simulated particles is approximately 10^5, which results in feasible computation times. For the simulations at the chosen friction velocities this corresponds to minimum scale factors of $\psi_{\mathrm{min}} = 20, 500, 750, 1000, 1500$. A refinement factor of $\lambda = 5$ is used for the surface meaning that the grid size equals $\Delta x^{\mathrm{s}} = \Delta y^{\mathrm{s}} = 1\ cm$.

Table 1
LES settings

$\Delta x = 5\ cm$	$\Delta y = 5\ cm$	$\Delta z = 2\ cm$
$L_x = 8\ m$	$L_y = 4\ m$	$L_z = 4\ m$
$t^{\mathrm{spin}} = 5\ min$	$t^{\mathrm{sim}} = 20\ min$	$\Delta z_0 = 10\ cm$
$u_* = 0.3, 0.4, 0.5, 0.6, 0.7\ m/s$		$z_{0m}^{\mathrm{spin}} = 0.75, 1, 1.25, 2, 2.5\ mm$

Table 2
Saltation settings

$d = 0.25\ mm$	$\rho^{\mathrm{p}} = 2650\ kg/m^3$	$\chi = 0.05$
$\phi = 0.4$	$\zeta^{\mathrm{p}} = 0.15$	$\zeta^{\mathrm{s}} = 0.3$
$z_{0m}^{\mathrm{s}} = 0.01\ mm$	$C^T = 0.111$	$\gamma^T = 2.9 \cdot 10^{-4}\ N/m$
$\lambda = 5$	$\Delta x^{\mathrm{s}} = 1\ cm$	$\Delta y^{\mathrm{s}} = 1\ cm$
$\psi_{\mathrm{min}} = 20, 500, 750, 1000, 1500$		$\alpha = 45$ degrees

4. Results and Discussion

The results for $u_* = 0.5\ m/s$ are shown in detail after which they are compared with the results for different large scale pressure gradients. Figure 5 shows a video/snapshot of the last 5 minutes of the simulation at 2 times real speed. Two slabs of the turbulent wind field, as obtained by the LES, are shown in blue. A mass concentration is obtained from the locations of the saltating particles, which is shown in yellow. The LES surface topography, $\langle h \rangle$, is shown in copper. Lighter colors correspond to higher values. The wind direction is towards the lower left corner. Figure 5 shows that saltation is very heterogeneous in space and time.

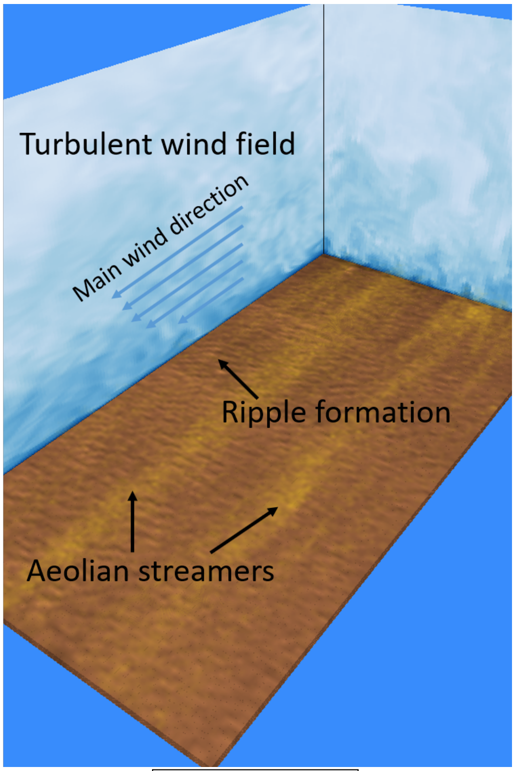

Figure 5: Snapshot/video of the last 5 minutes of the simulation at two times real speed. The turbulent wind field obtained from the LES model is shown in blue, the saltation concentrations obtained from the SLP model are shown in yellow and the LES surface height obtained from the HRS model is shown in copper. Lighter colors correspond to higher values. The wind direction is towards the lower left corner of the figure.

The transport takes place in elongated structures oriented parallel to the main wind direction. These aeolian streamers, as they are called, were also found in previous research (Baas and Sherman, 2005). The heterogeneity of the saltation is closely related to the heterogeneity of the turbulent wind field and the ability to resolve aeolian streamers is a direct consequence of the coupling between the resolved turbulent wind field and the individual sand particles.

The fluctuations in time are shown in fig. 6, which shows the time series of the horizontally averaged wind speed at the lowest height level, $z = 1\ cm$, the total concentration of sand in saltation and the average LES surface roughness, z_{0m}. During the first minutes of the simulation a rapid decrease of the average surface roughness is found, which indicates that the randomly perturbed surface is adapting quickly to the new conditions. During this period the random perturbations are flattened, which decreases the overall roughness. As a result an increase in the wind speed is witnessed. After a couple of minutes a positive trend is found for the surface roughness, which is an indication that new structures are being formed on the surface. The increasing roughness height slows down the wind field. The roughness height keeps increasing during the simulation, which indicates that the surface is not in equilibrium with the wind field and saltation flux. It can also be seen that the average LES roughness is two orders larger than the HRS subgrid roughness z^s_{0m}. The LES roughness, z_{0m}, is thus determined by the surface structures resolved in the HRS model rather than by the roughness of the individual grains (9). The wind field fluctuations on a smaller time scale are the result of turbulence. On these time scales large fluctuations in the saltating mass are found. The large peaks represent bursts of transported mass in the form of aeolian streamers.

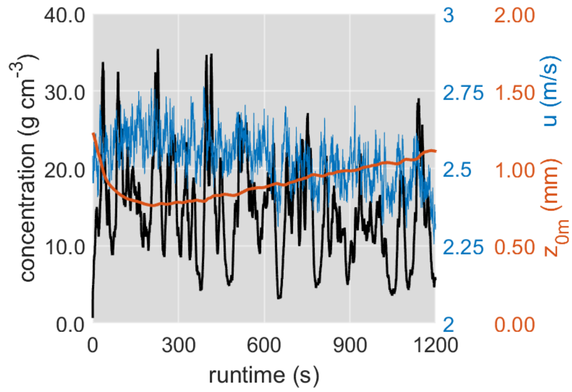

Figure 6: Timeseries of the domain averaged lowest height level wind speed, $z = 1\ cm$, (blue) mass in saltation (black) and surface roughness (red).

To further investigate the fluctuations present in the wind field and saltating mass concentration, C, and a potential coupling between both, normalised power spectral density plots are created for both signals, fig. 7. The spectra are normalised by their total power and are visualised on a double logarithmic scale. To mitigate spectral leakage both signals are windowed with a Hanning window. The power spec-

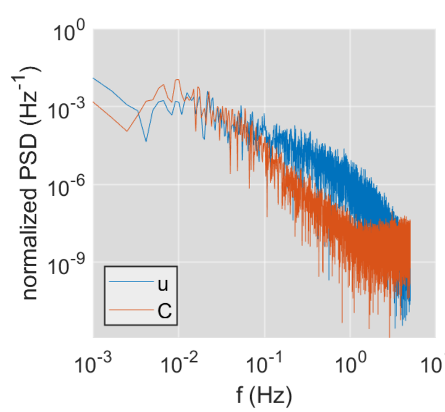

Figure 7: Normalised power spectral density plot of the mass in saltation (red) and lowest height level wind speed (blue). The spectra are normalised by their respective total power.

trum of the wind speed shows the expected behaviour for a turbulent flow. In line with Kolmogorov's theory, Kolmogorov (1941), turbulent kinetic energy is created on the macro scale and cascades towards smaller scales until dissipation takes over. For frequencies smaller than approximately 1 Hz the spectrum of the concentration shows a very similar behaviour, which demonstrates the tight coupling between the two and suggests that the turbulent variations in the wind field are responsible for the variations in the saltating mass. The similarity could be used to obtain information about saltation fluctuations from the turbulent spectrum. For frequencies above 1 Hz the spectra of the concentration no longer decays, but stays roughly constant. This is an indication that at these frequencies the saltation mass no longer obtains its energy from the turbulent structures. The fluctuations in the wind field with frequencies larger than 1 Hz fluctuate too fast for the saltating mass to adjust to. This corresponds to previous research, which generally states that the response time scale is in the order of seconds (Ma and Zheng, 2011) and strengthens the argument that subgrid turbulence will not have a significant influence on the saltating particles. The energy in the signal of the saltating mass at these frequencies, which is 6 orders of magnitude smaller than the energy present at the lower frequencies, could come from the surface initialisation scheme.

To further investigate the response time, a cross-correlation plot is constructed. Figure 8 shows the cross-correlation coefficient, G, for the wind field at the lowest height level and the saltation concentration for different time offsets, t'. The correlation coefficients are calculated with a moving window of 30 seconds. The windowed data is detrended to remove the effects caused by the surface roughness. The black line is a smoothed line trough the maxima of the absolute cross-correlation coefficients. It can be seen that positive cross-correlation coefficients are mainly found for positive time offsets and negative cross-correlation coefficients for negative time offsets. The positive correlation for positive time offsets describes the feedback mechanism in which higher wind speeds can transport more sand. The time offset indicates the time the saltating mass needs to adjust to the wind field. The negative correlation for negative time offsets describes the retardation of the wind field due to an increased saltating mass. The time offset represents the response time of the wind field. It can be seen that both mechanisms play an important role, which demonstrates the benefit of having a two-way coupled model. The time scale on which the coupling takes place is in the order of seconds, which agrees with the deviation found around 1 Hz, in the turbulence and concentration power spectra, fig. 7.

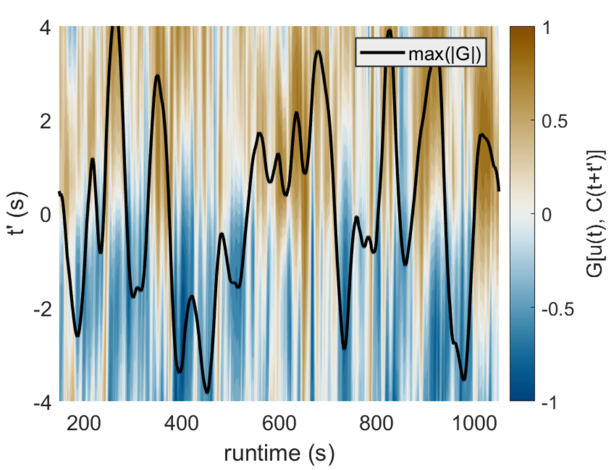

Figure 8: Cross-correlation coefficient, G, contour plot for the lowest height level wind speed, $z = 1\ cm$, and the total mass in saltation for different time offsets, t'. The correlation is obtained with a 30 seconds window. The x axis shows the centre of the window and the y axis the time offset between the wind velocity and the saltating mass. The maxima of the absolute coefficients are shown by the black line.

A shear stress balance is constructed using the turbulent shear stress given by the LES and the particle shear stress obtained by integrating the particle drag force, (17). The shear stress profile is averaged over the last 5 minutes of the simulation. We also constructed a mass flux profile for this time period. The mass flux is obtained with a linear fit through mass accumulated in discrete height bins. The total height integrated mass flux, q_{tot}, is given as well. The slope of the

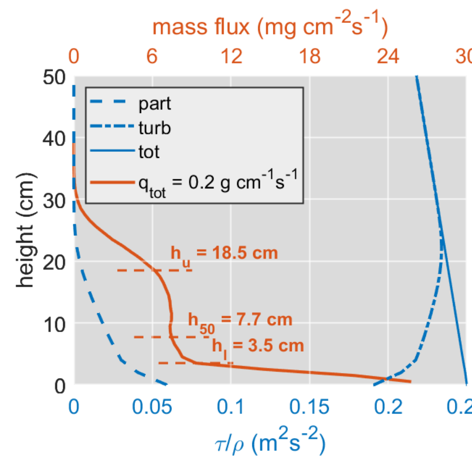

Figure 9: Shear stress balance (blue), showing the particle induced (part) shear stress, the turbulence induced shear stress (turb) and the total shear shear stress (tot). The slope of the total shear stress corresponds to the imposed large scale pressure gradient, indicating that the wind field and mass flux are in equilibrium. The mass flux profile is shown in red. q_{tot} is the total height integrated mass flux. Three heights are diagnosed, the height of the lower and upper layer, h_l & h_u, which are defined by the maximum and minimum of the second derivative of the profile. The commonly used height below which 50% of the mass flux takes place is also indicated, h_{50}.

total shear stress is constant and the resulting force cancels the imposed large scale pressure gradient. Over the averaged time period the wind field is thus in equilibrium with the imposed large scale pressure gradient and the saltation layer. Although the direct influence of the saltation layer is confined to the lower regions of the domain, $z < 40\ cm$, the information about the retarded wind field will be transferred upwards by the turbulent eddies and slow down the wind field above the saltation layer as well. The found total mass flux, q_{tot} agrees well with the values found by previous research, which were summarized by Kok et al. (2012) and will be discussed in more detail when we compare the results of the different simulations. The shape of the mass flux profile shows a bimodal behaviour. A distinct lower layer is visible with a height of h_l in which most of the mass flux takes place. Above the lower layer an upper layer can be seen. The upper layer is associated with the aeolian streamers. The accompanied high wind speed eddies lift a fraction of the particles higher up into the wind field, transporting them over longer distances with higher velocities. The heights of the upper and lower layer are defined by respectively the maximum and minimum of the second derivative of the mass flux profile. For comparison the height below which 50% of the mass flux takes place, h_{50}, is also marked, as this height is commonly used to define the saltation layer height. The different saltation layer heights will be compared to previous research when we discuss the different simulations.

To investigate the importance of different energy sources, an energy balance is constructed for the saltation layer, fig. 10. The balance is constructed by tracking the potential and kinetic energy changes of each individual simulated particle. The saltating particles obtain energy from the wind field via the drag force, E_{D}, and via surface initialisation, E_{S}. Energy is lost when they impact the surface, E_{I}. The total energy gain/loss is given by the sum of these three, E_{T}. Energy transferred via initialisation by splashing is not shown, as it acts neither as a sink nor source. It can be seen that

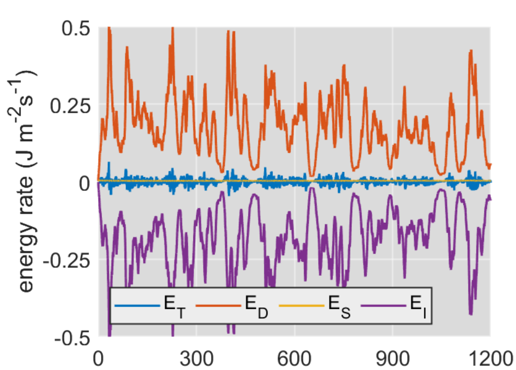

Figure 10: Energy balance for the saltating system. Energy is obtained from the wind field via the drag force, E_{D}, and via surface initialisation, E_{S}. The particles loose energy on impact, E_{I}. Initialisation by splashing is not shown as it acts neither as a source nor sink. The sum is shown by the total energy rate, E_{T}.

the drag force contribution is a much larger than the wind initialisation contribution. This was expected as previous research found that saltation is mainly driven by splash initialisation and not by wind initialisation (Kok et al., 2012). It also shows that the derived parametrisation for wind initialisation, (16), and the choice of χ will not have a significant impact on the results.

Figure 11 shows a video/snapshot of the surface evolution obtained from the HRS model at 10 times real speed. The top window shows a top-view section of the domain and the bottom window shows a $3D$ close-up view of the formation and growth of ripples. The first signs of ripple for-

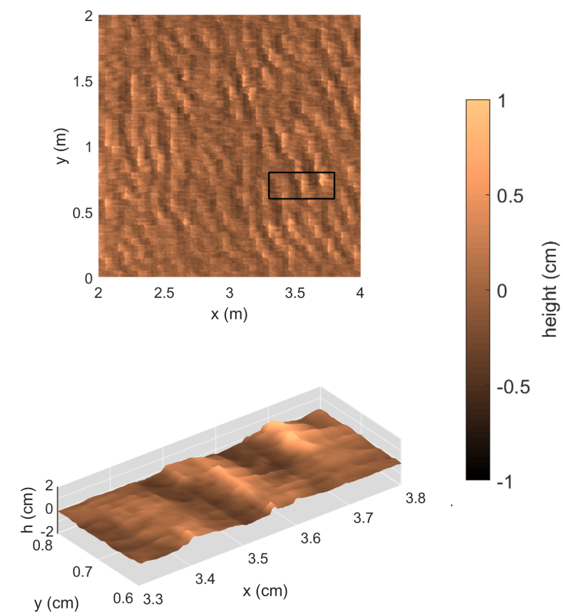

Load→Play/Pause

Figure 11: Surface evolution obtained with the HRS model. Top window shows a top-view section of the domain and bottom window shows a $3D$ close-up view of the ripples.

mation are found after 3 minutes, which corresponds to the increasing roughness found in fig. 6. It takes some time for the ripples to build and after 10 minutes of simulation time they are clearly visible. During the rest of the simulation they grow bigger and get more distinct. Previous research has shown that it can take up to an hour for ripples to reach their final equilibrium wavelength and shape (Manukyan and Prigozhin, 2009). This was however not the scope of this research. Andreotti et al. (2006) argues that slope stability is the growth limiting factor. To be able to study the growth of ripples to their equilibrium shape it could therefore be necessary to implement slope stability requirements into the model as the only growth limiting factor present now is the increased surface shear stress.

To investigate the properties of the surface structures a spatial Fourier analysis of the surface is conducted . Figure 12 shows a one dimensional spatial Fourier analysis that is obtained in the along wind direction on a semi logarithmic graph. The spectrum is an average of the spectra obtained for every along wind line during the last 5 minutes of the simulation. The surface ripples in fig. 11 are visible around

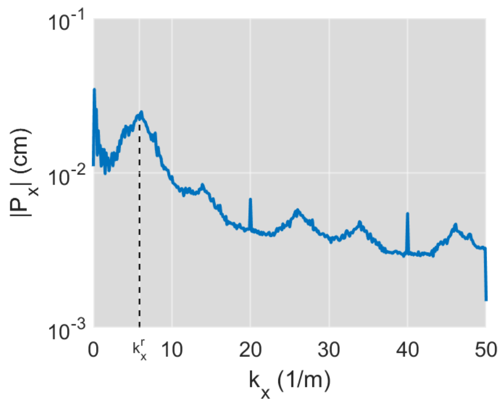

Figure 12: $1D$ spatial Fourier spectrum of the surface in the along wind direction. The spectrum is an average of all the $1D$ along wind direction spectra of the last 5 minutes of the simulation. The dominant ripple wavelength is found to be around $k_x^r = 5.88\ m^{-1}$.

$k_x^r = 5.88\ m^{-1}$. This corresponds to a ripple wavelength of approximately 17 cm. The large amplitudes near $k_x = 0$ are the result of a small trend that has developed on surface. The two narrow peaks at $k_x = 20\ m^{-1}$ and $kx = 40\ m^{-1}$ coincide with one and two times the LES grid resolution and can be considered an artifact. The height of the ripples is defined as the 95$^{\text{th}}$ height percentile of surface at the end of the simulation and equals 0.25 cm.

Figure 13 shows the total mass flux, q_{tot}, for all simulations (diamonds) together with the results from parametrisations found by previous research, which were summarised by Kok et al. (2012). The results of the parametrisations are for a particle diameter of $d = 0.25\ mm$ and an impact threshold friction velocity of $u_{*\text{it}} = 0.2\ m/s$. The simulated results are in the range of values predicted by the large-scale parametrisations. For large friction velocities, $u_* >> u_{*\text{it}}$, the parametrisations differ in their u_* dependence. Durán et al. (2011) predicts a quadratic dependence, while the other parametrisations (Bagnold, 1941; Kawamura, 1951; Owen, 1964; Lettau and Lettau, 1978; Sorensen, 2004) predict a cubic dependence. Our simulations for $u_* \geq 0.5\ m/s$ seem to agree more with a cubic dependence of the mass flux on the friction velocity. The deviation from the cubic relation at low friction velocities seems to appear earlier for our simulations, as the mass flux starts to drop at a faster rate for $u_* < 0.5\ m/s$.

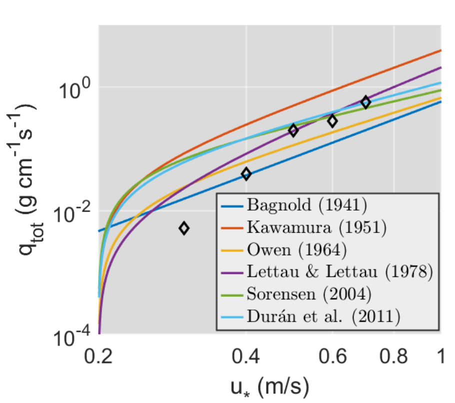

Figure 13: Mass flux, q_{tot}, for the different simulations (diamonds), together with parametrisations from previous research which were summarised by Kok et al. (2012).

Figure 14 shows the different saltation layer height definitions introduced in fig. 9 for the simulations together with the saltation layer height derived by Martin and Kok (2017) from the measurements of Namikas (2003). The results show that the top of the lower layer, h_l, is independent of the friction velocity. The upper layer is found for friction velocities of $u_* > 0.3\ m/s$ and increases rapidly in depth, h_u, for increasing friction velocities. This results in a gradual increase in h_{50}, the height below which 50% of the mass flux takes place. Previous research and field campaigns argue that the saltation layer height does not depend on the friction velocity and is around $3-5\ cm$ for a particle diameter of 0.25 mm (e.g. Kok et al., 2012; Martin and Kok, 2017). This corresponds to the height we find for the lower layer. The upper layer, which we see as a transitional phase between transport by saltation and suspension, is expected to grow with increasing wind speed as for very large wind speeds more particles would be transported in suspension higher up in the wind field. The signal of the upper layer would be difficult to measure as it is multiple times smaller than the signal of the lower layer and requires detailed measurements over a long height range. In addition, the signal is associated with aeolian streamers, which are heterogeneous in space and time, meaning that it is hard for equipment to capture sufficient of

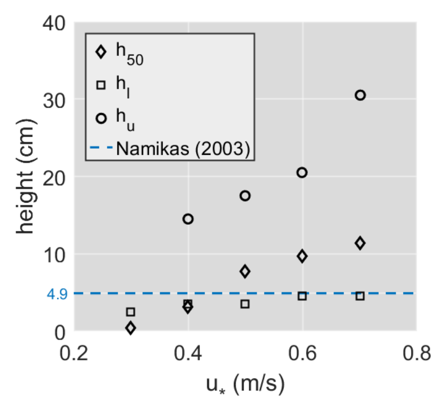

Figure 14: The height definitions introduced in fig. 9 for the the different simulations. The saltation layer height derived by Martin and Kok (2017) with the measurements of Namikas (2003) is also shown. For a friction velocity of $u_* = 0.3\ m/s$ no upper layer is found.

them. This could be the reason that measurement campaigns have not found the bimodal behaviour in mass flux profiles yet.

Figure 15 shows the wavelengths and heights of the ripples found in the simulations. The wavelengths found are in the same order as the wavelengths found in previous research (e.g. Andreotti et al., 2006; Manukyan and Prigozhin, 2009). It can be seen that the ripple height decreases rapidly with decreasing friction velocity, to the point that the ripples for $u_* \leq 0.4\ m/s$ are barely visible. The wavelengths seem to have a negative correlation with the friction velocity, which is in contradiction with previous research. The deviation could come from the missing slope stability requirements or from the fact that our ripples have not reached their final equilibrium shape yet. To study the formation of ripples longer simulations are required and more research is needed to investigate the mechanisms influencing the shape of the ripples.

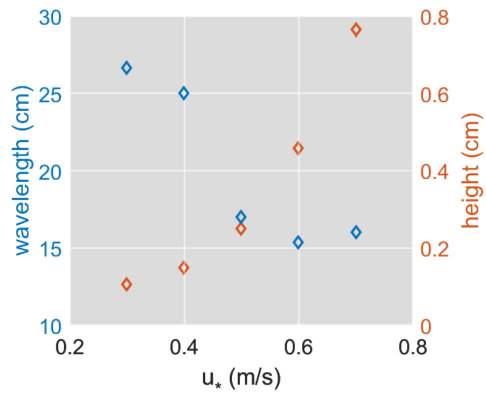

Figure 15: The dominant ripple wavelength and height found in the simulations. The height is defined as the 95$^{\text{th}}$ height percentile of the surface at the end of the simulation.

5. Conclusion

The combination of a scaled Lagrangian particle model, a large eddy simulation model and a high-resolution surface model developed in this research is found to be able to realistically simulate aeolian saltation in a turbulent wind field. The simulated transport takes place in aeolian streamers, which results in a highly heterogeneous mass flux signal in both space and time. The temporal frequency response of the total mass in saltation is found to have the same characteristics as the turbulence spectrum down to frequencies of 1 Hz, which indicates the strong coupling between the turbulent eddies and the saltating mass. Above 1 Hz the energy spectrum of the saltating mass no longer follows the decaying trend found in the turbulence spectrum. This is an indication that at these frequencies the energy supplied to the saltating mass, which is several orders of magnitude smaller than the energy present in the low frequency fluctuations, does not directly originate from the turbulent wind field, but rather from the surface initialisation scheme.

An equilibrium state is found when the results are averaged over a timescale that contains all important frequencies. In the equilibrium state the shear stress induced by the particles is compensated by a reduced turbulent shear stress, such that the sum of both results in a profile that opposes the imposed large scale pressure gradient. The averaged total mass flux found for these equilibrium states shows, for high wind velocities $u_* \geq 0.5\ m/s$, a cubic dependence on the imposed friction velocity.

The mass flux profile shows a bimodal behaviour. A lower layer is found with a height of 4 cm independent of the friction velocity. Above the lower layer an upper layer is found, which corresponds to transport taking place in aeolian streamers. The associated high wind speed eddies lift a fraction of the particles higher into the wind field where they are transported over larger distances at higher velocities. The upper layer is thought to be the result of a transitional phase between transport by saltation and suspension. This hypothesis is supported by the fast growth of the upper layer height with increasing friction velocity.

During the simulations ripples form and grow. No equilibrium state is found and an apparent negative correlation between the ripple wavelength and the imposed friction velocity seems to indicate that not all important physical mechanisms are present. To be able to study the formation of ripples in the future we therefore recommend the implementation of slope stability requirements into the high-resolution surface model and to conduct longer simulations. For more realistic field case studies we also recommend the implementation of a particle size distribution and the addition of heterogeneous impact and threshold conditions.

CRediT authorship contribution statement

FPA Liqui Lung: Conceptualization, Methodology, Software (Saltation & Surface), Formal analysis, Writing - Original Draft, Visualization. **S de Vries:** Writing - Review & Editing. **HJJ Jonker:** Supervision, Software (LES), Writing - Review & Editing.

References

Andreotti, B., Claudin, P., Pouliquen, O., 2006. Aeolian sand ripples: Experimental study of fully developed states. Physical review letters 96, 028001. doi:10.1103/PhysRevLett.96.028001.

Baas, A., Sherman, D., 2005. Formation and behavior of aeolian streamers. Journal of Geophysical Research (Earth Surface) 110, 3011–. doi:10.1029/2004JF000270.

Bagnold, R., 1941. The Physics of Blown Sand and Desert Dunes. doi:10.1007/978-94-009-5682-7.

Creyssels, M., Dupont, P., Ould El Moctar, A., Valance, A., Cantat, I., Jenkins, J., Pasini, J., Rasmussen, K., 2009. Saltating particles in a turbulent boundary layer: Experiment and theory. Journal of Fluid Mechanics 625, 47 – 74. doi:10.1017/S0022112008005491.

Durán, O., Claudin, P., Andreotti, B., 2011. On aeolian transport: Grain-scale interactions, dynamical mechanisms and scaling laws. Aeolian Research 3, 243–270. doi:10.1016/j.aeolia.2011.07.006.

Gillette, D., 1974. On the production of soil wind erosion aerosols having the potential for long range transport. J. Rech. Atmos. 8, 735–744.

Goossens, W.R., 2019. Review of the empirical correlations for the drag coefficient of rigid spheres. Powder Technology 352. doi:10.1016/j.powtec.2019.04.075.

Goudie, A., 2020. Dust Storms and Human Health. pp. 13–24. doi:10.1007/978-3-030-23773-8_2.

Heus, T., van Heerwaarden, C., Jonker, H., Siebesma, A., Axelsen, S., Dries, K., Geoffroy, O., Moene, A., Pino Gonzalez, D., Roode, S., Arellano, J., 2010. Formulation of the dutch atmospheric large-eddy simulation (dales) and overview of its applications. Geoscientific Model Development, v.3, 415-444 (2010) 3. doi:10.5194/gmd-3-415-2010.

Ho, T., Valance, A., Dupont, P., Ould El Moctar, A., 2011. Scaling laws in aeolian sand transport. Physical review letters 106, 094501. doi:10.1103/PhysRevLett.106.094501.

Huang, N., He, P., Zhang, J., 2020. Large-eddy simulation of sand transport under unsteady wind. Geomorphology 358, 107105. doi:10.1016/j.geomorph.2020.107105.

Iversen, J., Rasmussen, K., 1999. The effect of wind speed and bed slope on sand transport. Sedimentology 46, 723 – 731. doi:10.1046/j.1365-3091.1999.00245.x.

Jickells, T., An, Z., Andersen, K., Baker, A., Bergametti, G., Brooks, N., Cao, J., Boyd, P., Duce, R., Hunter, K., Kawahata, H., Kubilay, N., Laroche, J., Liss, P., Mahowald, N., Prospero, J., Ridgwell, A., Tegen, I., Torres, R., 2005. Global iron connections between desert dust, ocean biogeochemistry, and climate. Science (New York, N.Y.) 308, 67–71. doi:10.1126/science.1105959.

Kawamura, R., 1951. Study of sand movement by wind. Translated (1965) as University of California Hydraulics Engineering Laboratory Report HEL 2-8, Berkeley .

Kok, J., Parteli, E., Michaels, T., Francis, D., 2012. The physics of wind-blown sand and dust. Reports on progress in physics. Physical Society (Great Britain) 75, 106901. doi:10.1088/0034-4885/75/10/106901.

Kok, J., Rennó, N., 2006. Enhancement of the emission of mineral dust aerosols by electric forces. Geophysical Research Letters - GEOPHYS RES LETT 33. doi:10.1029/2006GL026284.

Kok, J., Rennó, N., 2009. A comprehensive numerical model of steady state saltation (comsalt). Journal of Geophysical Research (Atmospheres) 114, 17204–. doi:10.1029/2009JD011702.

Kolbuszewski, J., Nadolski, L., Dydacki, Z., 1950. Porosity of wind-deposited sands. Geological Magazine 87, 433 – 435. doi:10.1017/S001675680007744X.

Kolmogorov, A.N., 1941. The local structure of turbulence in incompressible viscous fluid for very large reynolds numbers. Translated (1991) as proceedings of the Royal Society of London 434, 9–13. doi:10.1098/rspa.1991.0075.

Kroy, K., Sauermann, G., Herrmann, H., 2002. Minimal model for sand dunes. Physical review letters 88, 054301. doi:10.1103/PhysRevLett.88.054301.

Lettau, K., Lettau, H., 1978. Experimental and micro-meteorological field studies of dune migration, exploring the world's driest climate. IES Report 101, University of Winsconsin-Madison, Institute for Environmental Studies, Madison, USA , 110–147.

Li, B., Sherman, D., FARRELL, Ellis, J., 2010. Variability of the apparent von kármán constant during aeolian saltation. Geophysical Research Letters 37. doi:10.1029/2010GL044068.

Ma, G., Zheng, X.J., 2011. The fluctuation property of blown sand particles and the wind-sand flow evolution studied by numerical method. The European physical journal. E, Soft matter 34, 1–11. doi:10.1140/epje/i2011-11054-3.

Manukyan, E., Prigozhin, L., 2009. Formation of aeolian ripples and sand sorting. Physical review. E, Statistical, nonlinear, and soft matter physics 79, 031303. doi:10.1103/PhysRevE.79.031303.

Martin, R., Kok, J., 2017. Wind-invariant saltation heights imply linear scaling of aeolian saltation flux with shear stress. Science Advances 3. doi:10.1126/sciadv.1602569.

Miller, R., Tegen, I., Perlwitz, J., 2004. Surface radiative forcing by soil dust aerosols and the hydrologic cycle. Journal of Geophysical Research 109. doi:10.1029/2003JD004085.

Namikas, S., 2003. Field measurement and numerical modeling of aeolian mass flux distributions on a sand beach. Sedimentology 50, 303 – 326. doi:10.1046/j.1365-3091.2003.00556.x.

Obukhov, A., 1971. Turbulence in an atmosphere with non-uniform temperature. Boundary-Layer Meteorology 2, 7–29. doi:10.1007/BF00718085.

Owen, P., 1964. Saltation of uniform grains in air. Journal of Fluid Mechanics 20, 225 – 242. doi:10.1017/S0022112064001173.

Richter, D., Dempsey, A., Sullivan, P., 2019. Turbulent transport of spray droplets in the vicinity of moving surface waves. Journal of Physical Oceanography 49. doi:10.1175/JPO-D-19-0003.1.

Sauermann, G., Kroy, K., Herrmann, H., 2001. A continuum saltation model for sand dunes. Physical review. E, Statistical, nonlinear, and soft matter physics 64, 031305. doi:10.1103/PhysRevE.64.031305.

Schalkwijk, J., Jonker, H., Siebesma, A., Meijgaard, E., 2015. Weather forecasting using gpu-based large-eddy simulations. Bulletin of the American Meteorological Society 96, 715–723. doi:10.1175/BAMS-D-14-00114.1.

Shao, Y., 2008. Physics and Modelling Wind Erosion. volume 23.

Shao, Y., Lu, H., 2000. A simple expression for wind erosion threshold friction velocity. Journal of Geophysical Research 105, 22437–22444. doi:10.1029/2000JD900304.

Shao, Y., Raupach, M., Findlater, P., 1993. Effect of saltation bombardment on the entrainment of dust by wind. Journal of Geophysical Research 98, 12719–12726. doi:10.1029/93JD00396.

Sherman, D., Li, B., 2012. Predicting aeolian sand transport rates: A reevaluation of models. Aeolian Research 3. doi:10.1016/j.aeolia.2011.06.002.

Shima, S.i., Kusano, K., Kawano, A., Sugiyama, T., Kawahara, S., 2009. The super-droplet method for the numerical simulation of clouds and precipitation: a particle-based and probabilistic microphysics model coupled with a non-hydrostatic model. Quarterly Journal of the Royal Meteorological Society 135, 1307 – 1320. doi:10.1002/qj.441.

Sorensen, M., 2004. On the rate of aeolian sand transport. Geomorphology 59, 53 – 62. doi:https://doi.org/10.1016/j.geomorph.2003.09.005. aeolian Research: processes, instrumentation, landforms and palaeoenvironments.

Sullivan, P., McWilliams, J., Moeng, C.H., 1994. A subgrid-scale model for large-eddy simulation of planetary boundary-layer flows. Boundary-Layer Meteorology 71, 247–276. doi:10.1007/BF00713741.

Tomas, J., Pourquie, M., Jonker, H., 2015. The influence of an obstacle on flow and pollutant dispersion in neutral and stable boundary layers. Atmospheric Environment 113. doi:10.1016/j.atmosenv.2015.05.016.

Tong, D., Huang, N., 2012. Numerical simulation of saltating particles in atmospheric boundary layer over flat bed and sand ripples. Journal of Geophysical Research (Atmospheres) 117, 16205–. doi:10.1029/2011JD017424.

Vries, S., Southgate, H., Kanning, W., Ranasinghe, R., 2012. Dune behavior and aeolian transport on decadal timescales. Coastal Engineering 67, 41–53. doi:10.1016/j.coastaleng.2012.04.002.

de Vries, S., Thiel de Vries, J., Rijn, L., Arens, S., Ranasinghe, R., 2014. Aeolian sediment transport in supply limited situations. Aeolian Research 12, 75–85. doi:10.1016/j.aeolia.2013.11.005.

Westerweel, J., Boersma, B., Nieuwstadt, F., 2016. Turbulence. doi:10.1007/978-3-319-31599-7.

Wyngaard, J., 2011. Turbulence in the Atmosphere. volume 64. doi:10.1017/CBO9780511840524.